Research Square

Preprints are preliminary reports that have not undergone peer review.
They should not be considered conclusive, used to inform clinical practice,
or referenced by the media as validated information.

Coupled-resonator-enabled active–passive control of Kerr solitons for tunable and low-noise frequency synthesis

Dongmei Huang

meihk.huang@polyu.edu.hk

Photonics Research Institute, Department of Electrical and Electronic Engineering, The Hong Kong Polytechnic University

Jie Xu
Huanjie Cheng
Helin Jiang
Feng Li
Yihuan Shi

Article

Keywords:

Posted Date: September 14th, 2026

DOI: https://doi.org/10.21203/rs.3.rs-10691559/v1

License: This work is licensed under a Creative Commons Attribution 4.0 International License.
Read Full License

Additional Declarations: There is **NO** Competing Interest.

Coupled-resonator-enabled active–passive control of Kerr solitons for tunable and low-noise frequency synthesis

Jie Xu[1,2], Huanjie Cheng[1,2], Helin Jiang[1,2], Feng Li[2], Yihuan Shi[1,2,*], and Dongmei Huang[1,2,*]

[1] *Photonics Research Institute, Department of Electrical and Electronic Engineering, The Hong Kong Polytechnic University, Hong Kong*

[2] *The Hong Kong Polytechnic University Shenzhen Research Institute, Shenzhen 518057, China*

**Corresponding Authors, Email: shiyihuan1994@163.com;meihk.huang@polyu.edu.hk*

Abstract

Dissipative Kerr soliton (DKS) in optical microresonators with wide-range repetition-rate tunability and ultra-low timing noise is significant for precision metrology, microwave and optical frequency synthesis. However, increasing the repetition rate tunability will shorten the soliton existence step and degrade noise performance. Here, we propose a unified active–passive control method by utilizing an engineered dispersive wave (DW) as a second controller to achieve broad repetition-rate tuning with low timing noise. Through mode hybridization in a coupled-resonator system, deterministic DW emission generates a controllable spectral recoil that enables broad repetition-rate tuning and compensates for the Raman self-frequency shift, leading to a stationary zero-drift operating point. Furthermore, this identical DW resonance acts as an orthogonal port for active stabilization. Targeted continuous-wave injection at the DW mode establishes a robust optical trapping potential via cross-phase modulation. Numerical simulations reveal that this localized trap effectively confines the soliton's random-walk motion, suppressing low-frequency timing fluctuations by nearly 59 dB. This ultralow-noise operation requires an auxiliary power fraction of only ~2%, thereby preserving the primary soliton existence range. This work provides a way to generate reconfigurable, ultra-low-noise integrated microcombs by engineering the tunability and stabilization of the Kerr generation dynamics.

Introduction

Dissipative Kerr soliton (DKS) generated in high-Q optical microresonators has emerged as a transformative platform for precision metrology, optical frequency synthesis and low-noise microwave generation [1–7]. In these applications, both deterministic, wide range tunability of the repetition rate and robust suppression of intrinsic timing noise is highly desirable to achieve optimal performance. Existing approaches typically focus on optimizing just one feature at a time. It is still challenging to simultaneously optimize both features as expanding the repetition-rate tuning range will deteriorate the noise performance, or vice versa.

Regarding repetition-rate control, wide-range tuning in single-resonator platforms is conventionally realized by adjusting the cavity's refractive index via thermo-optic, direct electro-optic (EO), or piezoelectric (PZT) modulation [8–12]. However, thermo-optic approaches have limited tuning speed [13–15], fast tuning via PZT (e.g., in AlN or Si_3N_4 integrated actuators) [16] or EO modulation (e.g., in lithium niobate) [8,17] have problems in altering the effective cavity detuning and

intracavity energy. Besides, the proposed tuning methods will disturb the balance of dispersion-nonlinearity and loss-gain as the cavity resonance shifts against the fixed pump laser and the soliton is easily pushed out of its narrow existence detuning range. Alternatively, passive coupled-cavity engineering through Vernier-effect geometries expands the parameter space via mode hybridization [18–26]. However, these schemes typically introduce discrete hopping in the repetition rate rather than smooth, continuous tuning, and they also lack an active mechanism to suppress the timing noise originating from fundamental thermal noise [27].

For highly stable Kerr comb generation in microresonators, several methods have also been proposed to reduce the timing noise [28–33]. Operating at a localized quiet point, where thermodynamic noise and Raman self-frequency shifts cancel each other out [34], locks the soliton to a fixed cavity detuning and eliminates its tunability. Alternatively, external optoelectronic phase-locked loops can dynamically stabilize the repetition rate [35], but they require bulky, power-consuming, high-speed microwave components that goes against the purpose of compact microcomb integration. All-optical approaches rely on active optical trapping, such as amplitude-modulated pumping or the injection of an auxiliary continuous-wave (CW) laser into an adjacent primary comb mode [20,36,37]. In conventional single ring configurations, establishing an optical trapping potential deep enough to effectively pin the soliton requires substantial auxiliary pump power. This strong secondary field induces severe nonlinear crosstalk such as strong cross-phase modulation (XPM) background and unwanted four-wave mixing (FWM) sidebands along with thermal shifts within the resonator. These thermal and nonlinear perturbations dynamically distort the effective cavity detuning and power balance, thereby narrowing the soliton step. Consequently, robust temporal stabilization is achieved at the cost of a compressed and fragile existence range, restricting simultaneous attempts at dynamic repetition-rate tuning.

To address the inherent limitations of conventional soliton tuning and trapping techniques, this work proposes and theoretically verifies an active-passive collaborative control framework. The developed framework enables simultaneous realization of continuous parameter tuning and stable trapping of solitons while rigorously maintaining the soliton existence conditions. Our core innovation lies in completely decoupling soliton generation from its kinematic manipulation by utilizing a deterministically engineered dispersive wave (DW) as an orthogonal, dual-purpose control channel [38]. Evanescent coupling between the primary Kerr microresonator and a passive auxiliary ring cavity induces an avoided mode crossing (AMX) effect, which facilitates the generation of phase-locked DWs. The resulting DWs produce passive spectral recoil effects that support continuous repetition-rate tuning without disrupting the energy balance of the main cavity. Meanwhile, such DWs compensate the Raman self-frequency shift[34,39], enabling the system to operate at a stable zero-drift state. Notably, this passive DW engineering seamlessly accommodates active temporal stabilization. We demonstrate that by coherently injecting a low-power auxiliary CW laser strictly into the DW resonance, a robust optical trap via Kerr cross-phase modulation is

established. Analytically described by a stochastic Adler equation, this optical trap effectively restricts the random walk of solitons. This mechanism suppresses the low-frequency timing noise by nearly 59 dB, with the auxiliary laser power accounting for merely 2–5% of the main pump power. The developed active-passive control framework establishes a unified strategy to reconcile wide-range tunability and ultra-low-noise operation. Benefiting from the non-intrusive control mechanism, the soliton existence range and frequency comb conversion efficiency are almost unaffected. This work provides a promising pathway toward the development of reconfigurable, high-performance integrated frequency comb sources.

Results

Section 1: Deterministic Dispersive Wave Emission via Mode Hybridization

A coupled-microresonator architecture is proposed for dispersion engineering and active–passive control of Kerr soliton dynamics, as shown in Fig. 1a. The system comprises a Kerr-nonlinear main microresonator driven by a continuous-wave (CW) pump and evanescently coupled to a passive auxiliary ring resonator. The effect of the auxiliary resonator on the resonance spectrum of the main cavity is depicted in Fig. 1b. In the absence of coupling, the resonance frequencies of the main cavity are indicated by the blue dots, while the gray dashed line represents an equidistant frequency grid determined by the pumped resonance and the free spectral range (FSR) of the main cavity. When a resonance of the auxiliary ring is tuned into the vicinity of a longitudinal mode of the main resonator, strong coupling between the two resonators leads to mode hybridization and generates a localized avoided mode crossing (AMX). Consequently, the resonance frequencies are shifted from their unperturbed positions, yielding the perturbed supermode spectrum represented by the red dots. These modified resonance frequencies will tailor the integrated dispersion of the coupled-microresonator.

The integrated dispersion is defined as $D_{\mathrm{int}}(\mu) = \omega_\mu - (\omega_0 + D_1\mu)$, where μ is the relative mode number with respect to the pumped resonance, D_1 is the cavity free spectral range, and ω_μ is the resonance frequency of mode μ. For an isolated single-ring resonator, the integrated dispersion is dominated by second-order group-velocity dispersion and follows the familiar parabolic dependence $D_{\mathrm{int}} \approx D_2\mu^2/2$, as shown by the blue dashed curve in Fig. 1c. Using the perturbed resonance frequencies obtained from the coupled-resonator eigenmodes, we calculate the modified integrated dispersion profile, as shown by the red dots in Fig. 1c. The localized deviation from the original parabolic background is a direct consequence of the AMX-induced resonance shift. To isolate the effect of mode hybridization, the green curve shows the dispersion perturbation introduced by the AMX, defined as the difference between the perturbed and unperturbed integrated-dispersion profiles. This localized spectral defect constitutes a key mechanism for deterministic dispersive-wave emission.

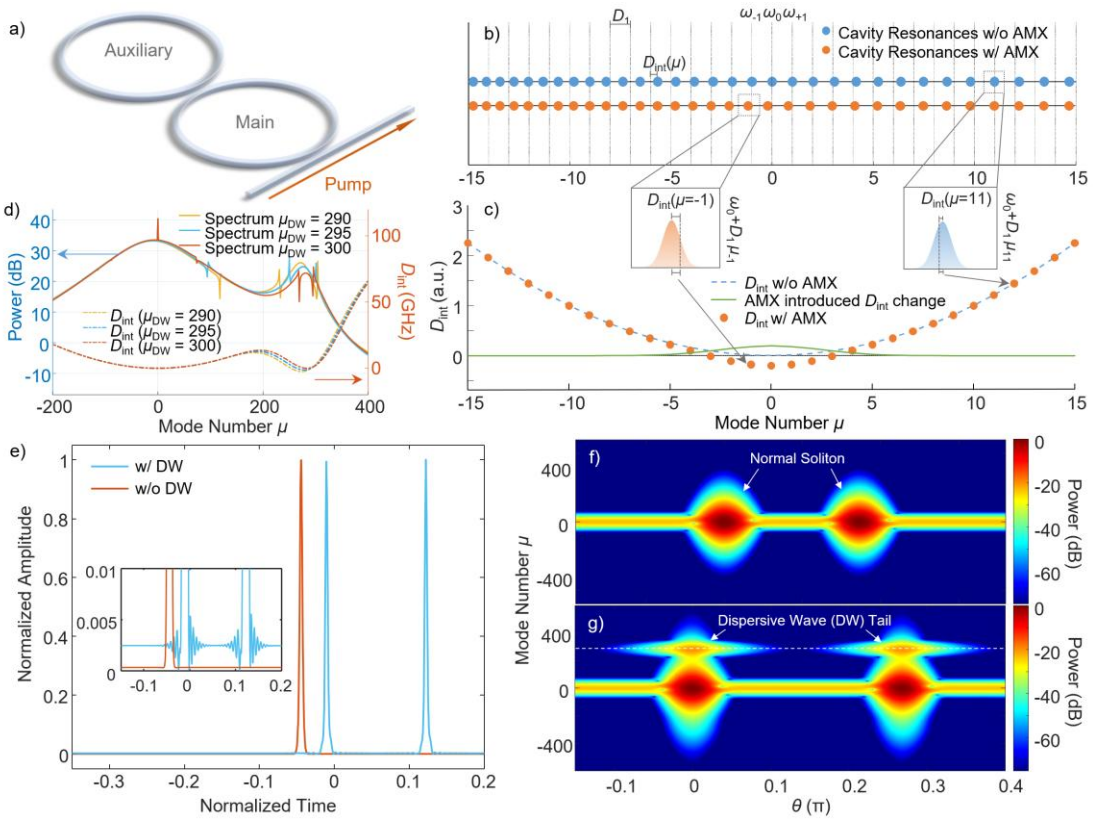


Fig. 1 | Principle of deterministic dispersion engineering and dispersive wave emission. (a) Schematic of the coupled dual-ring microresonators system. (b) Resonance frequency distribution without (blue dots) and with (orange dots) mode splitting induced by the auxiliary resonator. (c) Integrated dispersion D_{int} profiles showing the unperturbed parabolic dispersion (blue dashed line), the perturbed dispersion (red symbols), and the localized dispersion modification induced by the AMX (green curve, representing the difference between the perturbed and unperturbed states). (d) Simulated soliton spectra and corresponding D_{int} profiles under varying coupling conditions. (e) Temporal waveforms of an unperturbed soliton (orange curve) and a DW-engineered soliton (blue curve); the inset shows a magnified view of the trailing oscillatory tail. (f, g) Time-frequency spectrograms of (f) an unperturbed soliton and (g) DW-engineered soliton, demonstrating that the temporal oscillations originate from localized radiation at the phase-matched mode index μ_{DW}.

To model the nonlinear dynamics of Kerr solitons with the engineered dispersion via mode hybridization, we use a generalized Lugiato–Lefever equation (LLE). The slow time t evolution of the intracavity field envelope $A(\tau, t)$ in the main resonator, defined in the co-moving frame (fast time τ), is governed by [21,26]:

$$t_R \frac{\partial A}{\partial t} = \left[-\frac{\kappa}{2} - i\delta_0 + i \sum_{k\geq 2} \frac{D_k}{k!} \left(i \frac{\partial}{\partial \tau} \right)^k + i\gamma L \mid A \mid^2 \right] A + \sqrt{\kappa_{\mathrm{ex}} t_R P_{\mathrm{in}}} + \mathcal{F}^{-1}\{\hat{f}(\mu)\tilde{A}(\mu, t)\}, \quad (1)$$

where t_R is the round-trip time, κ is the total loss rate, $\delta_0 = \omega_0 - \omega_p$ is the pump-resonance detuning, L is the cavity length, D_k are the k-th order integrated dispersion coefficients (mapping

directly to the physical dispersion parameters $\beta_k L$), γ is the Kerr nonlinear parameter, κ_{ex} is the external coupling rate, and P_{in} is the input pump power. The operator $\hat{J}(\mu) = i\delta\omega_{AMX}(\mu)$ represents the frequency-dependent inter-cavity coupling induced by the auxiliary resonator, typically defined as a localized complex frequency perturbation. Applied in the frequency domain via the Fourier transform $\tilde{A}(\mu, t) = \mathcal{F}\{A(\tau, t)\}$, it directly incorporates the engineered AMX effect into the nonlinear cavity dynamics.

Numerical simulations show that tuning the resonance frequency of the auxiliary resonator continuously shifts the AMX position and correspondingly displaces the phase-matched DW frequency. As shown in Fig. 1d, the generated DW peak follows the AMX position throughout the entire tuning range, enabling deterministic control of the DW frequency. The influence of the engineered DW emission also substantially modifies the temporal soliton profile. Compared with the ideal sech^2 pulse profile of an unperturbed dissipative Kerr soliton, the DW-carrying soliton develops a pronounced oscillatory tail trailing the main pulse (Fig. 1e), which constitute a characteristic signature of coherent DW emission.

To verify the origin of these temporal oscillations, we performed a time–frequency analysis of the intracavity field. The spectrograms as shown Figs. 1f and 1g indicate that the oscillatory energy is strongly localized around μ_{DW}. This observation confirms that the trailing oscillation originates from a coherent DW component that remains phase-locked to the soliton rather than from incoherent background fluctuations. By breaking the spectral and temporal symmetry of the soliton, the emitted DW induces a momentum imbalance. To satisfy momentum conservation, the DW exerts a continuous spectral recoil on the soliton. As discussed in the following sections, this spectral recoil provides the physical mechanism for passive repetition-rate control, while the engineered DW mode serves as the foundation for active optical trapping dynamics.

Section 2: Broad repetition-rate tuning and Raman self-frequency shift compensation via deterministic DW emission

2.1 Orthogonal control of broad repetition-rate tuning

The deterministic DW emission induced by AMX provides an effective pathway to control the kinematic properties of dissipative Kerr solitons. Since the soliton is a coherent, phase-locked nonlinear excitation, the emission of a localized DW results in an asymmetric redistribution of spectral energy. Momentum conservation requires a compensating recoil of the soliton spectrum, leading to a shift in its spectral center of mass (CoM). The soliton CoM frequency can be expressed as $\Omega_c = \mu_c \cdot D_1$, where the relative spectral mode number center μ_c is given by [40,41]:

$$\mu_c = \frac{-i}{4\pi E}\int_{-\pi}^{\pi}\left(A^*\frac{\partial A}{\partial \phi} - A\frac{\partial A^*}{\partial \phi}\right)d\phi. \quad (2)$$

Here, E is the total intracavity energy, A is the intracavity complex field envelope, and Φ is the co-moving angular coordinate. Through the anomalous group-velocity dispersion of the resonator, a

shift of the spectral CoM is directly converted into a change in the soliton group velocity. Assuming that the velocity response is dominated by second-order dispersion, the resulting repetition-rate variation is given by [18,39,41]:

$$\frac{\Delta f_{\mathrm{rep}}}{f_{\mathrm{rep}}} = \frac{D_2}{D_1^2}\Delta\Omega_c \,, \tag{3}$$

where $f_{\mathrm{rep}} \approx D_1/2\pi$. This relation establishes a direct connection between the engineered DW recoil and repetition-rate control. A notable feature of this tuning mechanism is that the perturbation remains spectrally localized around the engineered DW mode. A s a result, the global pump–soliton locking condition is preserved, allowing substantial repetition-rate tuning without destabilizing the soliton existence range.

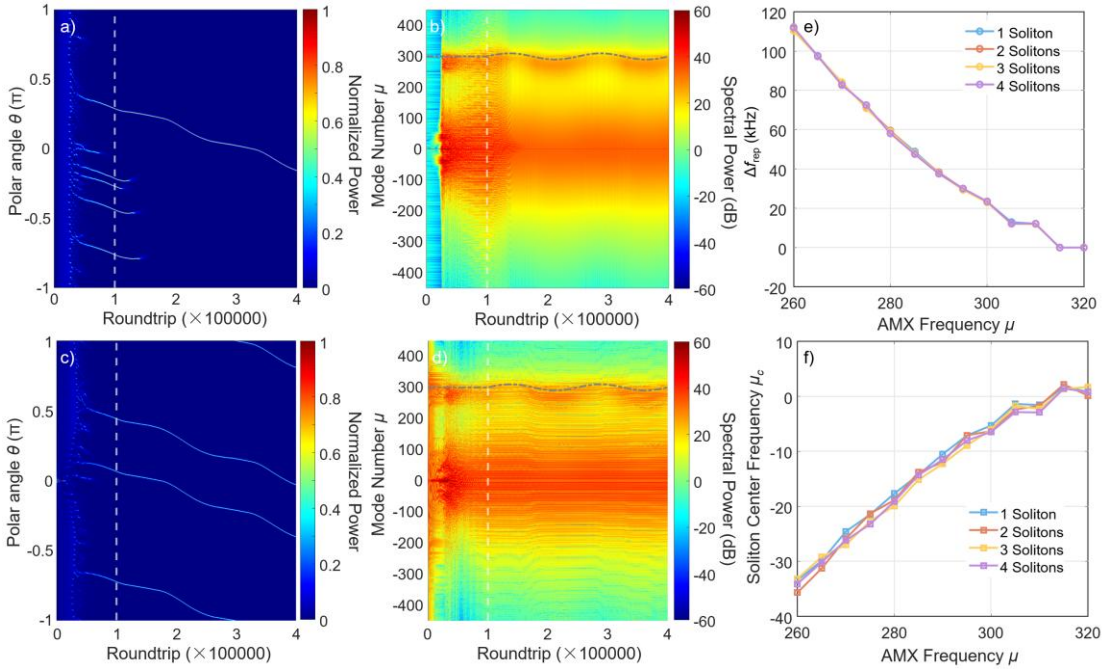


Fig. 2 | Kinematic control via DW emission. (a) Time-domain, and (b) frequency-domain evolution profiles of a single-soliton state. Dynamically shifting the AMX frequency (gray dashed line in b) modulates the DW position, inducing a controllable tilt in the temporal soliton trajectory (a), demonstrating deterministic FSR manipulation. (c) Time-domain, and (d) frequency-domain evolution for a four-soliton state. Similar spectral tracking and temporal drift dynamics are observed despite the different soliton numbers. (e) Repetition-rate shift Δf_{rep} and (f) Spectral center-of-mass shift as functions of the AMX position for one-, two-, three-, and four-soliton states. The overlapping tuning curves indicate that the recoil-induced repetition-rate control is independent of the number and arrangement of solitons within the cavity.

To validate this dynamic repetition rate control mechanism, we performed numerical simulations where the AMX position was with continuous sinusoidal modulation. Figures 2a and 2b show the corresponding temporal and spectral evolution of a single-soliton state. The DW frequency follows the AMX position throughout the tuning process, while the temporal soliton

trajectory exhibits a controllable tilt in the temporal window. Since the trajectory slope in the co-moving frame corresponds directly to the soliton group velocity, this observation confirms deterministic tuning of the repetition rate through DW recoil. This kinematic behavior is consistently observed in multi-soliton states. As illustrated in Figs. 2c and 2d, a four-soliton state exhibits nearly identical spectral tracking and temporal drift characteristics. This result indicates that the recoil force operates locally on each individual pulse envelope, independent of the number of coexisting solitons in the cavity.

The universality of this mechanism is verified in Figs. 2e and 2f. Decreasing the spectral separation between the main soliton and the AMX location (i.e., shifting μ_{DW} closer to the pump) enhances the spectral overlap with the {Citation}soliton envelope, thereby enhancing DW emission. The increase in DW power exerts a stronger spectral recoil, leading to larger shifts of both the spectral center of mass (CoM) and the repetition rate. Both the CoM displacement and the repetition-rate shift exhibit a nearly linear dependence on the AMX position. Notably, the tuning curves for one-, two-, three-, and four-soliton states are highly consistent. This independence confirms that the recoil-induced repetition-rate shift is governed by the localized dynamics of individual pulse envelopes rather than the spatial configuration or number of coexisting solitons inside the resonator.

The achievable tuning range is summarized in the tuning landscape shown in Fig. 3a. Larger repetition-rate shifts are obtained either by increasing the pump power or by reducing the spectral separation between the pump and the DW mode. Both effects increase the spectral overlap responsible for DW generation and therefore strengthen the recoil force. More importantly, this coupled architecture structurally decouples the soliton-generation channel (the main microresonator) from the tuning channel (the auxiliary ring). Consequently, manipulating the AMX position via the auxiliary cavity does not perturb the primary pump-cavity detuning or the thermal balance of the main ring. This separation preserves the stability of the soliton existence range, enabling broad repetition-rate tuning without driving the system out of its nonlinear locking regime. Besides, it also enables high-speed modulation, breaking the speed bottlenecks inherent to conventional tuning methods such as thermo-optic modulation constrained by thermal relaxation time. [14,42]. In contrast, the auxiliary resonator offers a pathway toward high-speed electro-optic or piezoelectric modulation, enabling rapid manipulation of the AMX position. To quantify the dynamic response, we evaluated the transfer function by applying high-frequency AC modulation to the AMX resonance frequency. The corresponding frequency response (Fig. 3a) exhibits a nearly flat response bandwidth extending into the megahertz regime. Corresponding time-domain evolution snapshots (Fig. 3b, insets A–B) confirm soliton tracking within this operational window. As the modulation frequency approaches the kinematic bandwidth limit (Fig. 3b, inset C), the soliton trajectory begins to distort and cannot maintain stable long-term synchronization with the driving signal. At even higher modulation frequencies (Fig. 3b, insets D–E), the imposed perturbation will induce severe trajectory distortion and cause the system to break its locking state with the modulation grid.

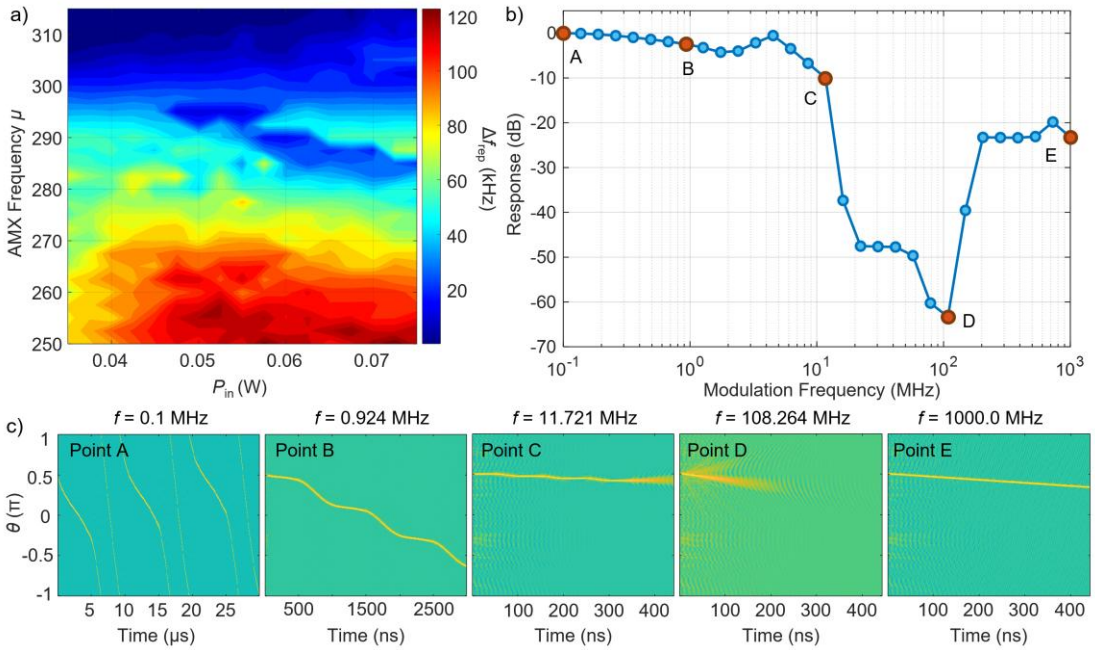


Fig. 3 | Dynamic tuning bandwidth and operational limits of spectral-recoil control. (a) Frequency response of the spectral CoM displacement under AC modulation of the AMX position, revealing a tuning bandwidth extending into the megahertz regime. (b) Time-domain soliton trajectories corresponding to the modulation frequencies marked A–E in (a), showing tracking (A, B), the onset of trajectory distortion near the bandwidth limit (C), and eventual tracking failure at higher frequencies (D, E). (c) Tuning landscape of the achievable repetition-rate shift as a function of pump power and the AMX frequency index. Larger tuning ranges are obtained at higher pump powers and smaller values of AMX frequency.

2.2 Raman self-frequency shift compensation via engineered DW recoil

The engineered DW emission also provides a way to compensate for Raman self-frequency shift, which acts as a persistent force that drives the spectral center of mass towards longer wavelengths and consequently adjusts the repetition rate. By introducing the deterministic DW emission, the temporal evolution of the soliton CoM frequency is governed by a force-balance equation [34,41]:

$$\frac{d\Omega_c}{dt} = F_{\mathrm{Raman}} + F_{\mathrm{Recoil}}, \tag{4}$$

where F_{Raman} and F_{Recoil} represent the effective forces exerted by the intrapulse Raman scattering and the engineered DW emission, respectively.

Figure 4a illustrates the individual and combined contributions of Raman scattering and the engineered DW emission. When only the Raman effect exists, the soliton experiences a continuous drift away from its initial operating point, producing the trajectory as shown by the red curve. In contrast, the DW emission acts in the opposite direction and generates the blue trajectory. By appropriately selecting the AMX position, the DW recoil can be tuned to exactly compensate for the Raman contribution such that $F_{\mathrm{Raman}} + F_{\mathrm{Recoil}} = 0$. Under this condition, the spectral CoM

reaches a stationary equilibrium, which is shown by the green trajectory in Fig. 4a. Unlike the isolated Raman or DW recoil cases, the balanced state remains localized around a stable zero-drift operating point over the entire simulation duration. This force-balanced equilibrium is illustrated via the spectral zoom near the pump resonance (Fig. 4e), the complete optical spectra (Fig. 4f), and the corresponding temporal profiles (Fig. 4g). With only Raman effect, intra-pulse Raman scattering continuously transfers energy to lower frequencies, displacing the soliton spectral CoM towards the long-wavelength side of the pump. In the anomalous group-velocity dispersion regime, this spectral redshift causes the pulse to decelerate, resulting in a continuous backward drift within the co-moving temporal window (red curve). Conversely, the DW recoil state introduces a spectral blueshift towards the short-wavelength side, which accelerates the soliton and induces an opposite, forward temporal shift (blue curve). When the Raman and DW recoil are perfectly balanced, the spectral CoM is realigned with the pump resonance, the velocity mismatch is eliminated, and the soliton remains perfectly stationary at the center of the temporal window, confirming the establishment of a stationary zero-drift state.

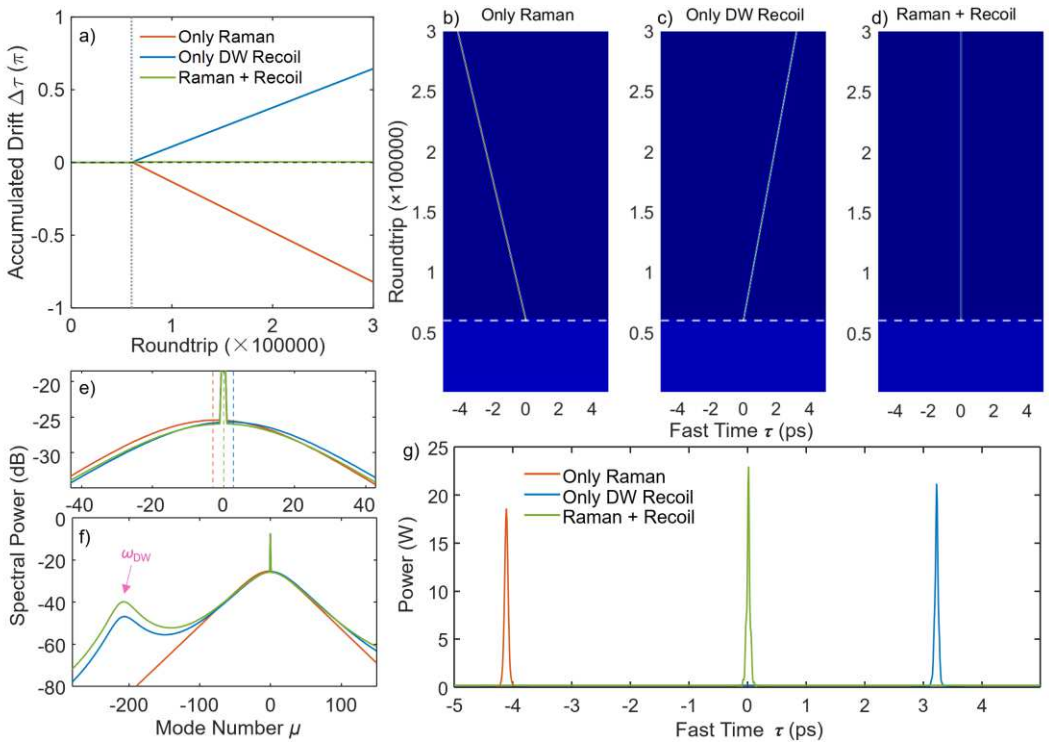


Fig. 4 | Raman self-frequency shift compensation via engineered DW recoil. (a) Temporal drift trajectories of single solitons simulated from identical initial noise seeds. The red and blue curves correspond to the Raman-only and DW-only cases, respectively, while the green curve tracks the stationary force-balanced state. (b)-(d) Long-term temporal evolution maps for the (b) Raman-only, (c) DW-only, and (d) Force-balanced states, respectively. (e) High-resolution spectral view around the pump resonance, with dashed lines indicating the calculated spectral CoM positions. (f) Corresponding full optical spectra and (g) Temporal pulse profiles for the three operating conditions.

The long-term temporal evolution maps as shown in Figs. 4b–d further demonstrate the effect of force balancing. The uncompensated states suffer from continuous walk-off relative to the co-moving frame, while the force-balanced soliton remains stationary. The engineered DW emission serves not only as a repetition-rate tuning mechanism but also as a passive stabilized element that suppresses intrinsic nonlinear drift without requiring external feedback.

Section 3: Active temporal trapping and low timing noise via dispersive-wave pumping

3.1 Soliton trapping and tweezing

The engineered DW emission also provides active control via pumping. To realize low-noise operation and deterministic positioning of solitons, we propose an active trapping mechanism based on resonant pumping of the engineered DW mode. A weak auxiliary continuous-wave (CW) laser is injected to excite the phase-matched DW resonance at the wavenumber of μ_{DW}. As illustrated in Fig. 5a, the activation of the auxiliary pump immediately suppresses the recoil-induced temporal drift of the soliton. Consequently, the soliton is stably confined at a fixed temporal position and fully locked to the co-moving reference frame. Once the auxiliary pump field is turned off, the soliton gradually restores its free-running dynamics and resumes the recoil-driven drift corresponding to the modified repetition rate. Notably, the auxiliary pump predominantly modulates the temporal position of the soliton rather than altering its existence conditions. As shown in Fig. 5b, the switch-on and switch-off of the auxiliary pump only introduces negligible perturbation to the intracavity energy, without inducing any measurable variation to the soliton existence threshold. This result verifies that the active trapping mechanism exerts minimal disturbance on soliton sustaining conditions, demonstrating an effective decoupling between soliton generation and precise soliton positioning.

The physical foundation of this trapping phenomenon relies on coherent intracavity interference. The auxiliary optical field coherently interferes with the intracavity background field sustained by the primary pump, generating a periodic spatial beat pattern along the resonant cavity. Through Kerr cross-phase modulation (XPM), such interference fringe induces periodic modulation of the intracavity refractive index, which constructs an effective optical potential well for soliton confinement. The effective potential can be theoretically expressed as[37,43]:

$$U(\tau_c) = -U_0 \cos(\mu_{DW}\tau_c + \phi_{\mathrm{aux}}), \tag{5}$$

where τ_c denotes the soliton temporal center, $U_0 = 2\eta\gamma\sqrt{P_{\mathrm{main}}P_{\mathrm{aux}}}$ represents the trap depth governed by the auxiliary pump power, η is the spatial overlap factor, and ϕ_{aux} is the relative phase of the auxiliary pump.

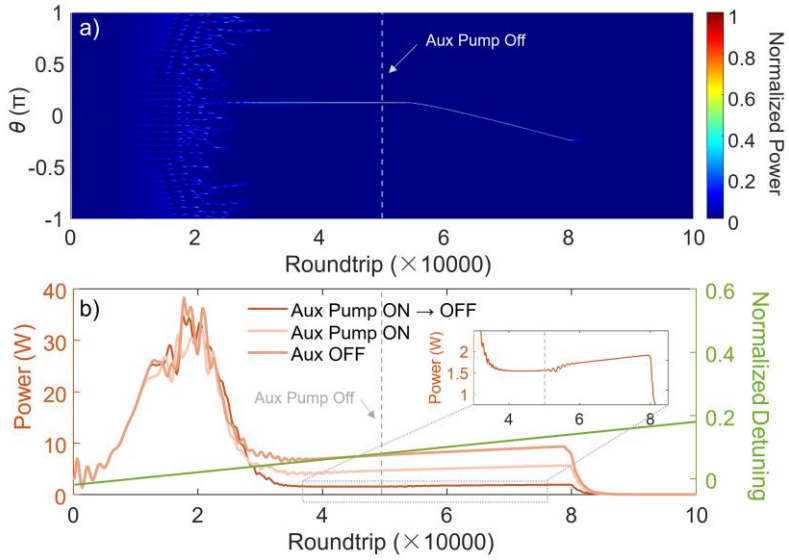


Fig. 5 | Active trapping and preservation of soliton existence. (a) Simulated time-domain evolution illustrating the temporal trapping of a dissipative Kerr soliton. The soliton trajectory remains tightly localized during the application of the auxiliary pump and progressively reverts to a free-running random-walk regime after the auxiliary field is removed (indicated by the dashed line). (b) Intracavity energy evolution for three operating conditions: continuous auxiliary pumping, no auxiliary pumping, and auxiliary-pump removal. The normalized pump detuning is shown on the right axis (green curve). The inset zooms in on the transient energy variations induced by switching the auxiliary pump off. The negligible perturbation confirms that temporal trapping does not significantly alter the soliton existence conditions.

By dynamically manipulating the phase of the auxiliary pump ϕ_{aux}, the periodic optical potential can be translated along the time domain. This controllable relocation of the trapped pulse is conceptually analogous to the 'temporal tweezing' technique previously demonstrated in fiber cavities [36]. We further conduct numerical investigations to characterize the dynamic trapping behavior throughout successive operational phases. As illustrated in Fig. 6, the entire process starts with soliton generation via frequency sweeping of the primary pump (Stage I). Once a stable soliton state is established, a linear phase scan from 0 to 2π is applied to the auxiliary pump (Stage II), which drives continuous displacement of the tailored potential well. The soliton precisely tracks this moving potential window, yielding a linear mapping between the auxiliary pump phase and the relative temporal coordinate of the pulse (Fig. 6b). To evaluate the robustness of the trap, a step phase jump from 2π back to 0 is subsequently introduced (Stage III). In response to the abrupt potential displacement, the soliton undergoes rapid acceleration and reliably re-locks to the relocated potential well within several cavity lifetimes. In the final stage (Stage IV), the auxiliary phase is fixed at a constant value, which permanently pins the soliton at the predefined temporal position and achieves stable static trapping.

In an ideal perturbation-free scenario, the soliton resides exactly at the minimum of the optical potential to minimize its effective intracavity energy. However, owing to the inherent spectral recoil induced by the engineered DW emission (as analyzed in Section 2), the soliton possesses an intrinsic kinematic drift. To counteract this continuous recoil force and sustain a stable locked repetition rate, the soliton settles at a steady-state equilibrium position that deviates slightly from the potential minimum. By resting on the gentle slope of the potential well, the soliton experiences an exact localized optical restoring force that perfectly balances the DW recoil drag, thereby achieving robust temporal trapping. The underlying mechanism is shown in Fig. 6c, where the soliton continuously follows the moving optical potential. Notably, rather than residing exactly at the minimum of the background optical potential, the soliton remains locked at a specific phase offset on the potential slope. This steady-state equilibrium is governed by two synergistic physical mechanisms. First, the soliton must climb slightly up the slope to generate a localized optical restoring force that perfectly neutralizes the intrinsic kinematic drag induced by the passive DW recoil (analyzed in Section 2). Second, the auxiliary pump is resonantly injected into the phase-matched DW mode and coherently interferes with the inherent DW field emitted by the soliton itself. Such coherent interference remodulates the effective optical potential perceived by the soliton and thereby shifts its equilibrium trapping position. Consequently, as $\phi_{\mathrm{aux}}$is varied, the soliton does not remain at a fixed offset from the potential minimum. Instead, the equilibrium offset evolves dynamically according to the instantaneous interference condition between the injected and soliton-generated DW fields. Importantly, the total intra-cavity energy remains nearly invariant throughout all four stages, as shown in Fig. 6d. Only a small and transient energy perturbation is observed immediately after the abrupt phase jump in Stage III, then the energy rapidly relaxes back to its original level. The inset of Fig. 6d highlights this transient response during the phase-jump event. The negligible energy variation throughout the entire manipulation sequence confirms that temporal tweezing operates largely independently of the thermodynamic energy balance that sustains the soliton state.

The results obtained from Figs. 5 and 6 demonstrate a core advantage of the proposed control strategy, namely the capability of manipulating soliton kinematic behaviors without substantially perturbing the soliton existence conditions. Conventional soliton control schemes typically implement modulation directly on the primary pump, which inevitably alters the cavity detuning state and intracavity energy level. Such intrinsic perturbations narrow the effective operating range for stable solitons and raise the risk of soliton annihilation. In contrast, the proposed dual-resonator configuration achieves physical decoupling between the soliton generation channel and the optical trapping channel, enabling nearly orthogonal regulation of soliton positional dynamics and soliton existence stability.

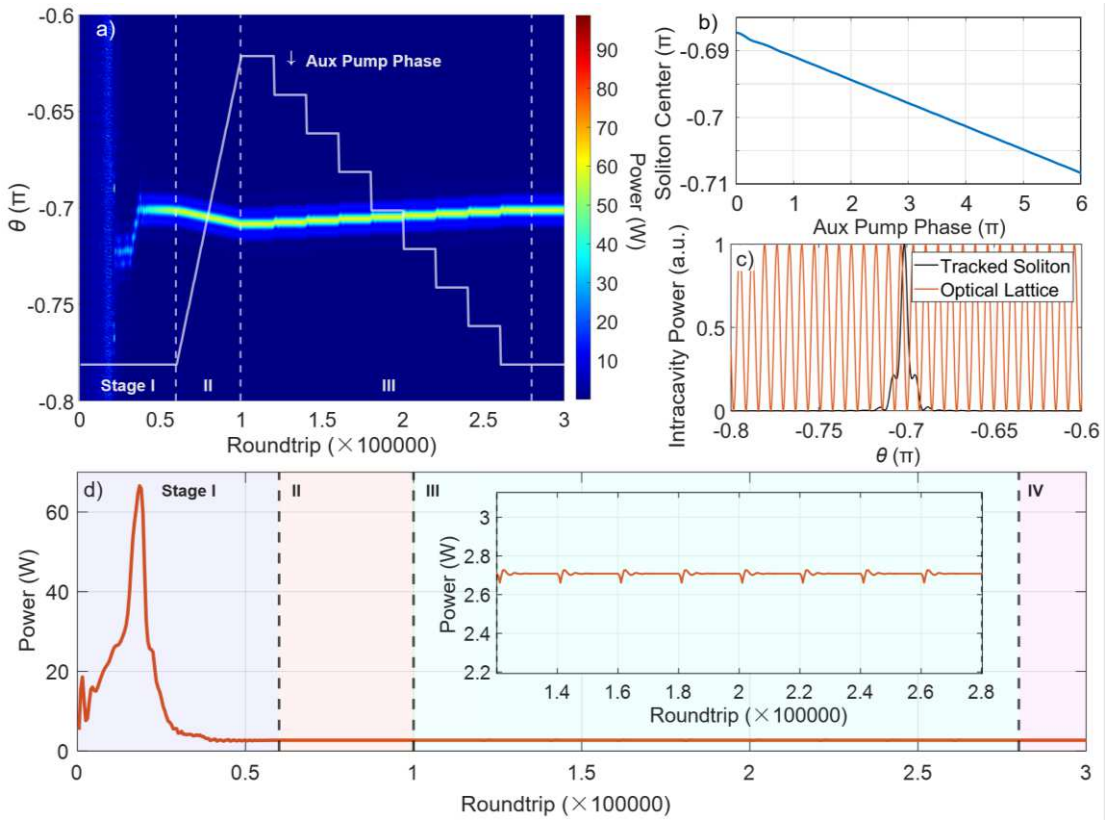


Fig. 6 | Temporal tweezing through phase-controlled optical trapping. (a) Stage I: soliton generation through primary-pump frequency sweeping. Stage II: linear scanning of the auxiliary-pump phase ϕ_{aux} (solid white line), from 0 to 2π. Stage III: abrupt phase reset from 2π to 0. Stage IV: fixed auxiliary phase. (b) Relative soliton position as a function of auxiliary-pump phase, demonstrating a linear phase-to-position transduction and deterministic control of the soliton temporal coordinate. (c) Schematic illustration of temporal tweezing. The soliton remains trapped at a finite phase offset from the minimum of the phase-controlled optical potential $U(\tau)$ formed by XPM-induced interference between the auxiliary field and the intracavity background. (d) Intracavity energy evolution continuously monitored across the successive operational stages: soliton generation via main pump frequency sweeping (light purple), linear phase scanning (pink), step-wise phase jumping (green), and static phase holding (rose). The negligible energy fluctuation proves that the temporal tweezing primarily affects the soliton position while leaving the underlying soliton existence conditions essentially unchanged.

We also analyze the dynamical bandwidth of the trapping mechanism. The tracking speed of this temporal tweezer is fundamentally constrained by the finite trapping stiffness, which is governed by the competition between the restoring force of the potential well and the velocity of the moving trap. Defining $\Delta\phi = \mu_{DW}\tau_c + \phi_{\mathrm{aux}}$ as the instantaneous relative phase difference between the soliton center and the potential minimum, the dynamics can be described by the Adler equation [37,44]:

$$\frac{d(\Delta\phi)}{dt} = -\Omega_{\text{trap}} \sin(\Delta\phi) + \Delta\omega, \tag{6}$$

where $\Delta\omega = d\phi_{\text{aux}}/dt$ is the instantaneous phase scanning rate (dragging speed) and $\Omega_{\text{trap}} = D_2 U_0 \mu_{DW}^2$ defines the maximum trapping bandwidth. When the dragging speed is within the trapping capability ($|\Delta\omega| < \Omega_{\text{trap}}$), the system possesses a stable locked solution, and the soliton remains synchronized with the moving potential. In contrast, if the phase modulation rate exceeds the maximum restoring force ($|\Delta\omega| > \Omega_{\text{trap}}$), phase locking can no longer be maintained, leading to phase slipping and eventual pulse escaping from the trap. This transition is characterized in Fig. 7. Representative temporal trajectories obtained at specific modulation frequencies (A–E) are shown in Fig. 7a. At low modulation frequencies, the soliton faithfully follows the potential trajectory. However, exceeding the dynamic threshold triggers a rapid roll-off in tracking fidelity (Fig. 7b), associated with continuously phase slipping, where the soliton escapes its current potential well and slips into adjacent cycles. Robust operation can be achieved over modulation bandwidths spanning from MHz to GHz.

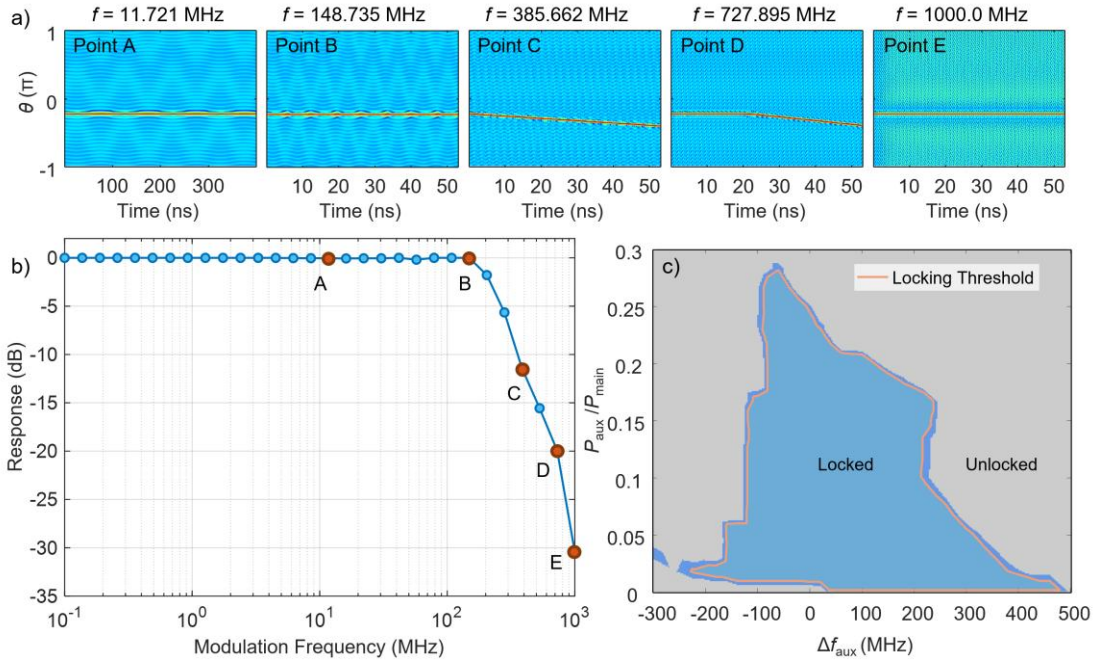


Fig. 7 | Dynamic trapping limits and locking phase diagram. (a) Time-domain soliton tracking snapshots corresponding to specific modulation frequencies (A-E) as the scanning speed approaches the dynamic threshold. (b) Tracking fidelity as a function of phase-scanning rate. A broad plateau is observed under stable locking, followed by a rapid roll-off associated with Adler unlocking and phase slipping. (c) Two-dimensional locking phase diagram as a function of auxiliary-pump frequency detuning from the DW resonance (horizontal axis) and auxiliary-to-main pump power ratio (vertical axis). The colored regions distinguish the dynamically locked and unlocked operating regimes. The boundary indicates the locking threshold, demonstrating the parameter space over which stable soliton trapping can be maintained.

To elucidate the full operational landscape of the trapping system, a two-dimensional locking phase diagram is shown in Fig. 7c, which is parameterized by the frequency detuning of the auxiliary pump relative to the DW resonance and the power ratio between the auxiliary and primary pumps. The color-coded domains explicitly differentiate the dynamically locked and unlocked operating regimes, wherein the distinct boundary quantitatively defines the critical locking threshold. This parametric mapping characterizes the valid working parameter space that supports stable, low-noise soliton trapping and precise temporal manipulation.

3.2 Adler-locked suppression of Gordon–Haus timing noise

The construction of the orthogonal control channel and the formation of a stable locking coordinate along the optical potential slope fundamentally reshape the stochastic noise dynamics of microcombs. Under free-running conditions, the temporal center of the soliton acts as a stochastic dynamical variable that is highly susceptible to intrinsic and environmental perturbations, including quantum noise, relative intensity noise (RIN), and thermo-refractive noise. In the absence of external confinement, these unregulated fluctuations induce a random-walk evolution of the soliton temporal position, leading to the characteristic $1/f^2$ timing-noise divergence known as the Gordon–Haus effect [41,45,46]. Activating the engineered DW trap introduces a localized optical potential that provides a restoring force against temporal displacement. The resulting dynamics are described by a stochastic Adler equation, which captures the competition between optical trapping and environmental noise [41,44–46]:

$$\frac{d(\Delta\phi)}{dt} = \Delta\omega - \Omega_{\text{trap}} \sin(\Delta\phi) + F_{\text{noise}}(t), \tag{7}$$

where $\Delta\phi$ is the relative phase coordinate, $\Delta\omega$ is the dragging speed, and $F_{\text{noise}}(t)$ represents the aggregate environmental noise driving force. Assuming the system is locked at a steady-state equilibrium phase $\Delta\phi_0$, the noise response of the system is fundamentally characterized by the effective locking bandwidth $\Omega_{\text{eff}} = \Omega_{\text{trap}}\cos(\Delta\phi_0)$.

The restoring force exerted by the optical trap fundamentally modulates the transfer characteristics of timing fluctuations to soliton dynamics. To quantitatively elucidate such noise suppression behavior, we perform a frequency-domain analysis based on the stochastic Adler equation and derive the corresponding noise transfer function [32,40]:

$$H_{\text{filter}}(f) = \frac{(2\pi f)^2}{(2\pi f)^2 + \Omega_{\text{eff}}^2}, \tag{8}$$

which defines the ratio of the phase-noise power spectral densities between the locked and free-running states. Equation (8) reveals that the optical trap induced by the auxiliary pump functions as a first-order high-pass filter for phase fluctuations. In the low-frequency regime ($2\pi f \ll \Omega_{\text{eff}}$), the power transfer function serves as $H_{\text{filter}} \propto f^2$ (corresponding to a linear f^1 amplitude scaling), indicating suppression of slow fluctuations. Physically, the restoring force continuously drives the soliton back towards its equilibrium position, prohibiting the long-term accumulation of timing

errors that dominates the free-running Gordon–Haus noise process. By contrast, high-frequency fluctuations far exceeding the locking bandwidth evolve too rapidly to be tracked and compensated by the trapping potential and thus remain nearly unattenuated.

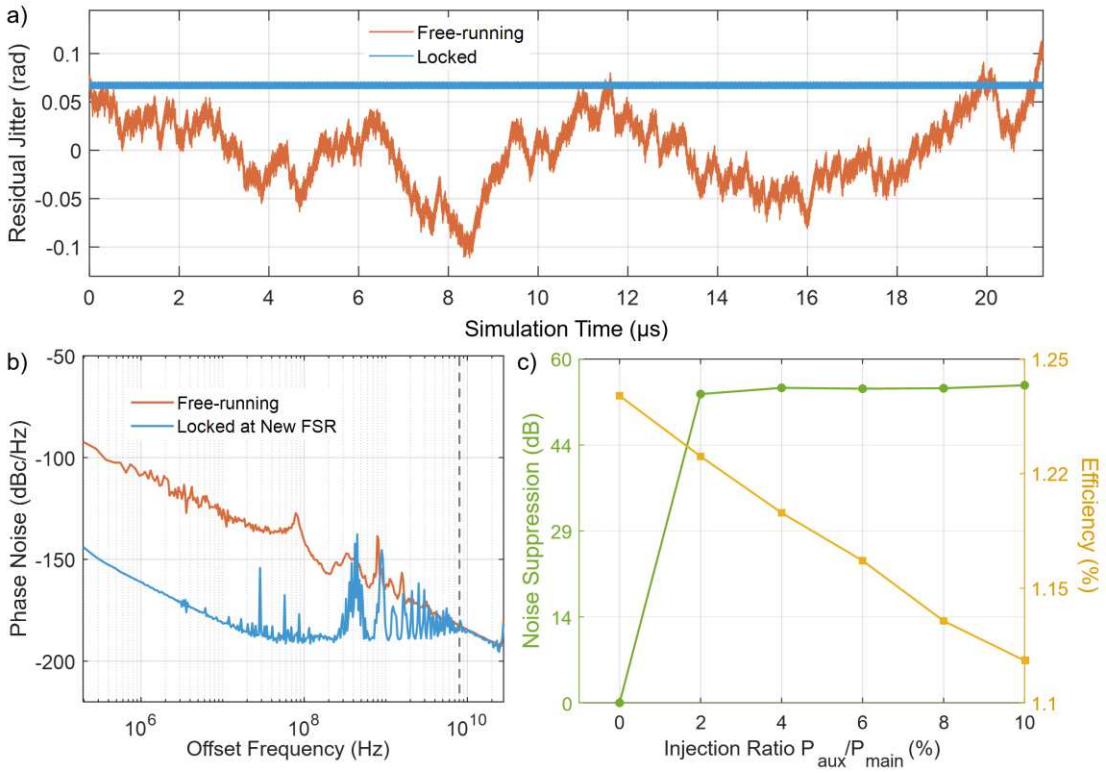


Fig. 8 | Simulated noise suppression and timing stabilization via active DW locking. (a) Residual phase jitter of the free-running and locked states. The free-running state exhibits large random-walk fluctuations arising from unconstrained timing diffusion, whereas the locked state remains tightly confined around a stable equilibrium position. (b) Simulated single-sideband phase-noise power spectral density (PSD) of the free-running and locked states. (c) Phase-noise suppression (green, left axis) and microcomb conversion efficiency (yellow, right axis) plotted against the auxiliary-to-main injection power ratio. Significant noise reduction is achieved with auxiliary-power fractions of only a few percent, while the comb conversion efficiency remains nearly unchanged.

To verify this noise-suppression mechanism predicted by the stochastic Adler analysis, we compare the stochastic timing fluctuations of the free-running and locked states through their residual phase jitter and corresponding phase-noise spectra. Figure 8a presents the residual phase jitter under the two operating conditions. In the free-running state without optical trapping, the system suffers from prominent low-frequency phase fluctuations originating from unconstrained Gordon–Haus timing noise. Such fluctuations accumulate continuously over time, generating a typical diffusive random-walk trajectory of the soliton phase. In contrast, activating the auxiliary pump enables stable soliton trapping at the tailored repetition rate, which substantially curbs the phase fluctuation amplitude and tightly confines the soliton phase around a stable equilibrium. The trapped state features a minor static phase offset of approximately 0.07 rad, which corresponds to

the steady-state soliton position within the optical potential well where the trapping restoring force fully balances the recoil-induced drift. Excluding this inherent equilibrium offset, the residual phase fluctuations are strongly constrained, verifying that the engineered optical trap effectively eliminates the long-term accumulation of timing errors.

This suppression is further reflected in the simulated single-sideband phase-noise spectra in Fig. 8b. While the free-running state exhibits the classic $1/f^2$ phase-noise dependence associated with random-walk timing fluctuations, the locked state shows a pronounced reduction of low-frequency phase noise. Consistent with the prediction of Eq. (8), the two spectra begin to diverge below the characteristic locking bandwidth (dashed line), where the optical trap effectively suppresses slow timing fluctuations. Above this frequency, the phase-noise spectra of the free-running and locked states largely overlap, indicating that fluctuations occurring faster than the trap response remain essentially unaffected. In this regime, the optical trap continuously restores the soliton towards its equilibrium position, thereby converting an unbounded random-walk process into a bounded fluctuation process. A phase-noise reduction of approximately 59 dB is obtained at an offset frequency of 150 kHz.

An additional advantage of the DW-assisted locking scheme is its high control efficiency. Figure 8c shows the phase-noise suppression (left axis) and comb conversion efficiency (right axis) as functions of the auxiliary-to-main pump power ratio $P_{\mathrm{aux}} / P_{\mathrm{main}}$. Increasing the auxiliary pump power enhances the optical trapping strength, thereby enabling progressive suppression of soliton phase noise. Remarkably, because the trap stiffness is leveraged by the square of the DW distance (μ_{DW}^2) rather than just the optical power, the large spectral separation of the engineered dispersive wave provides substantial leverage. Consequently, the noise suppression performance rapidly reaches a saturation plateau with an extremely low auxiliary power fraction of only 2%–5%. Throughout this effective working range, the microcomb conversion efficiency remains nearly invariant. These findings confirm that prominent timing noise reduction can be realized with negligible auxiliary power consumption, verifying the high efficiency of the proposed DW-assisted locking strategy for low-noise microwave signal generation.

Discussion and Conclusion

In conclusion, this work numerically establishes a unified active–passive control framework for dissipative Kerr solitons via tailored dispersive wave emission on a dual-resonator microcomb platform. Precise engineering of the AMX position enables deterministic DW generation at a predefined spectral location, which acts as a multifunctional channel for flexible soliton dynamic manipulation. Numerical simulations validate that the customized DW induces well-defined spectral recoil, facilitating continuous, wide-range tuning of the soliton repetition rate. Moreover, the recoil-derived counteracting force effectively compensates for the Raman self-frequency shift, yielding a stable stationary operating state that eliminates long-term spectral drift without relying on external feedback systems.

The engineered DW resonance further serves as an independent auxiliary optical injection channel. Resonant excitation of this DW mode constructs a customizable optical trapping potential, enabling deterministic soliton temporal positioning, phase-resolved temporal tweezing, and high-precision dynamic manipulation of soliton temporal coordinates. Benefiting from the large spectral separation between the primary pump and the tailored DW, the trapping stiffness is significantly enhanced. Strong soliton confinement can thus be realized with an extremely low auxiliary power ratio, achieving highly efficient regulation of soliton kinematic behaviors.

A core contribution of this work is the realization of orthogonal control between soliton generation and kinematic modulation. Traditional soliton manipulation strategies rely on direct primary pump modulation, which inevitably disturbs cavity operating conditions and compromises soliton stability. In contrast, the proposed platform physically decouples soliton generation, repetition-rate tuning, and optical trapping into independent functional channels. This structural separation enables precise repetition-rate modulation and temporal soliton positioning with negligible perturbation to intracavity energy distribution and soliton existence boundaries. Furthermore, the introduced optical trapping mechanism suppresses the inherent random-walk timing dynamics of free-running solitons and constrains phase fluctuations within a finite range, delivering prominent low-frequency timing noise reduction and substantially enhanced microwave signal stability.

This work proposes a single engineered dispersive-wave resonance to simultaneously realize passive repetition-rate control, Raman-drift compensation, and active temporal confinement. By combining force balancing at long timescales with optical trapping at short timescales, the framework provides a unified route for controlling soliton motion across multiple dynamical regimes. These results illustrate how dispersion engineering can be leveraged not only to shape soliton spectra, but also to engineer the effective forces acting on dissipative nonlinear states. This capability offers a general strategy for decoupling tunability from stability in microresonator frequency combs and may facilitate the development of agile, low-noise integrated sources for microwave photonics, coherent LiDAR, precision timing distribution, optical communications, and frequency-metrology applications. Beyond the specific dual-ring configuration investigated in this work, the underlying physical concept is general and adaptable to a wide range of nonlinear photonic resonators. In practical device applications, fabrication imperfections inevitably introduce static detuning offsets, which deviate the actual AMX spectral position from its theoretical design value. Such structural deviations can be effectively compensated via on-chip calibration strategies, for instance by employing integrated microheaters on the auxiliary resonator to precisely recalibrate the mode hybridization condition before device operation.

Author Contributions:

J.X., Y.S., and D.H. conceptualized the idea and designed the theoretical framework. J.X., H.C., and H.J. performed numerical simulations and theoretical calculations. J.X. and D.H. analyzed the data and wrote the original manuscript. F.L., Y.S., and D.H. contributed to the theoretical modeling and discussions. Y.S. and D.H. supervised the project. All authors discussed the results and contributed to the review and editing of the manuscript.

Declaration of competing interest: The authors declare that they have no known competing financial interests or personal relationships that could have appeared to influence the work reported in this paper.

Data Availability: The data that support the findings of this study are available from the corresponding authors upon reasonable request.

Acknowledgments: We acknowledge P. K. A. Wai for assistance in the work.

Funding: This work was supported by the Research Grants Council, University Grants Committee of Hong Kong SAR (PolyU25233024); and Start-up Fund for APs under the Strategic Hiring Scheme (P0046801).

REFERENCES

1. Kippenberg, T. J., Gaeta, A. L., Lipson, M. & Gorodetsky, M. L. Dissipative Kerr solitons in optical microresonators. *Science* **361**, eaan8083 (2018).
2. Diddams, S. A., Vahala, K. & Udem, T. Optical frequency combs: Coherently uniting the electromagnetic spectrum. *Science* **369**, eaay3676 (2020).
3. Spencer, D. T. *et al.* An optical-frequency synthesizer using integrated photonics. *Nature* **557**, 81–85 (2018).
4. Marin-Palomo, P. *et al.* Microresonator-based solitons for massively parallel coherent optical communications. *Nature* **546**, 274–279 (2017).
5. Kudelin, I. *et al.* Photonic chip-based low-noise microwave oscillator. *Nature* **627**, 534–539 (2024).
6. Liu, J. Photonic microwave generation in the X- and K-band using integrated soliton microcombs. *Nature Photonics* **14**, (2020).
7. Wu, K. *et al.* Vernier microcombs for integrated optical atomic clocks. *Nat. Photon.* **19**, 400–406 (2025).
8. He, Y. *et al.* High-speed tunable microwave-rate soliton microcomb. *Nat Commun* **14**, 3467 (2023).
9. Miao, R. *et al.* Repetition rate locked single-soliton microcomb generation via rapid frequency sweep and sideband thermal compensation. *Photon. Res.* **10**, 1859 (2022).
10. Wildi, T., Ulanov, A., Voumard, T., Ludwig, M. & Herr, T. Soliton Microcomb Repetition-Rate Locking via CW Laser Injection. in *2023 Conference on Lasers and Electro-Optics Europe & European Quantum Electronics Conference (CLEO/Europe-EQEC)* 1 – 1 (IEEE, Munich, Germany, 2023). doi:10.1109/CLEO/Europe-EQEC57999.2023.10231750.
11. Wang, Z. *et al.* Long-term repetition rate stabilization of soliton microcomb using optical closed-loop injection locking. *Optics & Laser Technology* **180**, 111549 (2025).

12. Niu, R. *et al.* Repetition rate tuning and locking of solitons in a microrod resonator. *Opt. Lett.* **49**, 570 (2024).
13. Li, J. *et al.* Thermal tuning of mode crossing and the perfect soliton crystal in a Si_3 N_4 microresonator. *Opt. Express* **30**, 13690 (2022).
14. Xue, X. *et al.* Thermal tuning of Kerr frequency combs in silicon nitride microring resonators. *Opt. Express* **24**, 687 (2016).
15. Bao, C. *et al.* Soliton repetition rate in a silicon-nitride microresonator. *Opt. Lett.* **42**, 759 (2017).
16. Liu, J. *et al.* Monolithic piezoelectric control of soliton microcombs. *Nature* **583**, 385–390 (2020).
17. Wang, C. *et al.* Monolithic lithium niobate photonic circuits for Kerr frequency comb generation and modulation. *Nat Commun* **10**, 978 (2019).
18. Bao, C. *et al.* Spatial mode-interaction induced single soliton generation in microresonators. *Optica* **4**, 1011 (2017).
19. Xue, X. *et al.* Normal‐dispersion microcombs enabled by controllable mode interactions. *Laser & Photonics Reviews* **9**, (2015).
20. Miller, S. A. *et al.* Tunable frequency combs based on dual microring resonators. *Opt. Express* **23**, 21527 (2015).
21. Helgason, Ó. B. *et al.* Dissipative solitons in photonic molecules. *Nat. Photonics* **15**, 305–310 (2021).
22. Xue, X., Zheng, X. & Zhou, B. Super-efficient temporal solitons in mutually coupled optical cavities. *Nat. Photonics* **13**, 616–622 (2019).
23. Jang, J. K. *et al.* Synchronization of coupled optical microresonators. *Nature Photon* **12**, 688–693 (2018).
24. Voloshin, A. S. *et al.* Dynamics of soliton self-injection locking in optical microresonators. *Nat Commun* **12**, 235 (2021).
25. Yang, Q.-F., Yi, X., Yang, K. Y. & Vahala, K. Spatial-mode-interaction-induced dispersive waves and their active tuning in microresonators. *Optica* **3**, 1132 (2016).
26. Zhu, K. *et al.* Power-efficient ultra-broadband soliton microcombs in resonantly-coupled microresonators. *Light Sci Appl* **15**, 185 (2026).
27. Stone, J. R. *et al.* Thermal and Nonlinear Dissipative-Soliton Dynamics in Kerr-Microresonator Frequency Combs. *Phys. Rev. Lett.* **121**, 063902 (2018).
28. Jin, X. *et al.* Microresonator-referenced soliton microcombs with zeptosecond-level timing noise. *Nat. Photon.* **19**, 630–636 (2025).
29. Huang, S.-W. *et al.* A broadband chip-scale optical frequency synthesizer at 2.7×10^{-16} relative uncertainty. *Sci. Adv.* **2**, e1501489 (2016).
30. Brochard, P., Schilt, S. & Südmeyer, T. Ultra-low noise microwave generation with a free-running optical frequency comb transfer oscillator. *Opt. Lett.* **43**, 4651 (2018).
31. Rolland, A., Egbert, S., Heffernan, B., Greenberg, J. & McGrew, W. Attosecond timing jitter in millimeter waves via Kerr optical frequency division. Preprint at https://doi.org/10.21203/rs.3.rs-8902301/v1 (2026).
32. Zhao, Z. *et al.* Optically locked low-noise photonic microwave oscillator. *National Science Review* nwag135 (2026) doi:10.1093/nsr/nwag135.
33. Kittlaus, E. A. *et al.* A low-noise photonic heterodyne synthesizer and its application to

millimeter-wave radar. *Nat Commun* **12**, 4397 (2021).
34. Yi, X. *et al.* Single-mode dispersive waves and soliton microcomb dynamics. *Nat Commun* **8**, 14869 (2017).
35. Tetsumoto, T. *et al.* Optically referenced 300 GHz millimetre-wave oscillator. *Nat. Photon.* **15**, 516–522 (2021).
36. Jang, J. K., Erkintalo, M., Coen, S. & Murdoch, S. G. Temporal tweezing of light through the trapping and manipulation of temporal cavity solitons. *Nat Commun* **6**, 7370 (2015).
37. Wildi, T., Ulanov, A., Voumard, T., Ludwig, M. & Herr, T. All-Optical Control of Soliton Microcomb Repetition-Rate through a Second CW Laser. in *2023 Conference on Lasers and Electro-Optics (CLEO)* 1–2 (2023).
38. Brasch, V. *et al.* Photonic chip–based optical frequency comb using soliton Cherenkov radiation. *Science* **351**, 357–360 (2016).
39. Karpov, M. *et al.* Raman Self-Frequency Shift of Dissipative Kerr Solitons in an Optical Microresonator. *Phys. Rev. Lett.* **116**, 103902 (2016).
40. Weng, W. *et al.* Spectral Purification of Microwave Signals with Disciplined Dissipative Kerr Solitons. *Phys. Rev. Lett.* **122**, 013902 (2019).
41. Jin, X., Lv, Z., Yao, L., Gong, Q. & Yang, Q.-F. Self-Suppressed Quantum-Limited Timing Jitter and Fundamental Noise Limit of Soliton Microcombs. *Phys. Rev. Lett.* **133**, 073801 (2024).
42. Joshi, C. *et al.* Thermally controlled comb generation and soliton modelocking in microresonators. *Opt. Lett.* **41**, 2565 (2016).
43. Taheri, H., Matsko, A. B. & Maleki, L. Optical lattice trap for Kerr solitons. *Eur. Phys. J. D* **71**, 153 (2017).
44. Moille, G. *et al.* Kerr-induced synchronization of a cavity soliton to an optical reference. *Nature* **624**, 267–274 (2023).
45. Matsko, A. B. & Maleki, L. On timing jitter of mode locked Kerr frequency combs. *Opt. Express* **21**, 28862 (2013).
46. Gordon, J. P. & Haus, H. A. Random walk of coherently amplified solitons in optical fiber transmission. *Opt. Lett.* **11**, 665 (1986).